sustainability

MDPI

Article

Development and Analysis of the Heliostat Curve Tracing Parametric Model (HCTPM) for Sustainable Solar Energy in Sun-Tracking Concentrated Solar Power Systems

Harnpon Phungrassami and Phairat Usubharatana *

Excellence Centre of Eco-Energy, Chemical Engineering Department, Thammasat School of Engineering, Thammasat University, Pathum Thani 12120, Thailand; pharnpon@engr.tu.ac.th
* Correspondence: uphairat@engr.tu.ac.th

Abstract: This study develops the heliostat curve tracing parametric model (HCTPM) to predict solar energy distribution in concentrated solar power (CSP) systems with sun-tracking capabilities. HCTPM uses curve tracing techniques to visualize flux distribution on mirrors and receivers, producing results that align closely with established models like HFLCAL, which use Gaussian and Tonatiuh ray-tracing methods. Simulations revealed that deviations in energy distribution increase as Sun shape error decreases, with greater impact on flux density and sensitivity. Variations in Sun disk radius caused notable deviations, especially in elliptical projections. The model's flexibility in adjusting mirror shapes and sizes allows for the evaluation of spill losses, optimizing mirror designs for different positions. Spill loss analysis showed that larger mirrors reduce spill loss on mirrors but increase it on receivers, particularly when mirrors deviate from the north. Although total spill loss decreases with larger mirrors, this effect weakens as receiver spill loss grows. These findings emphasize the importance of optimizing mirror and receiver design to maximize energy efficiency and minimize resource waste, contributing to more sustainable solar energy systems. The HCTPM model plays a crucial role in improving the sustainability of CSP systems by optimizing configurations based on Sun disk characteristics, reducing energy losses, and promoting efficient resource use.

Keywords: concentrated solar power (CSP); curve tracing; renewable energy; environmental parametric model

check for updates

Citation: Phungrassami, H.; Usubharatana, P. Development and Analysis of the Heliostat Curve Tracing Parametric Model (HCTPM) for Sustainable Solar Energy in Sun-Tracking Concentrated Solar Power Systems. *Sustainability* **2024**, *16*, 9214. https://doi.org/10.3390/su16219214

Academic Editors: Sergio Nardini and Firoz Alam

Received: 5 September 2024
Revised: 10 October 2024
Accepted: 16 October 2024
Published: 24 October 2024

Copyright: © 2024 by the authors. Licensee MDPI, Basel, Switzerland. This article is an open access article distributed under the terms and conditions of the Creative Commons Attribution (CC BY) license (https://creativecommons.org/licenses/by/4.0/).

1. Introduction

The demand for energy is expected to continue to grow over the next decade, driven by population growth and economic development. The catastrophic effect of pollution on the environment due to the use of fossil energy sources and the limitation of these sources, push us to look for a friendly and renewable energy source. Solar thermal technology is poised to play an important role as the cost of solar thermal systems has dropped dramatically, and the technology is becoming increasingly efficient [1]. The concentrated solar power (CSP) system is one type of solar technology, which generates solar power by using mirror or lenses (heliostat) to concentrate sunlight to a receiver. Among CSPs, the heliostat-central receiver configuration offers great potential in terms of power cycle efficiency, because it can reach the high temperature operating point (600 °C) with maximum conversion efficiency of 23–35% [2].

In order to enhance the effectiveness of radiant energy collection, it is imperative that heliostat deployment and solar tracking be suitably optimized and adjusted [3]. Predicting the radiative flux density distribution (RFDD) on the receiver surface is of significance for designing and deploying a central receiver system [4]. Uniform flux distribution is crucial for efficient energy collection, shadows, and thermal stresses that can compromise system components. Beyond efficiency, flux distribution analysis ensures system safety by

preventing overheating. Currently, there exist two primary methodologies to execute the simulation: the analytical methodology and the ray-tracing methodology [5].

Analytical methods offer computational speed and simplicity due to their reliance on straightforward mathematical expressions [6]. The intricacy of the present methodology stems from the numerous factors that dictate the flux spot, encompassing the direction of sunlight, shape of the Sun, and position, size, orientation, and surface slope error of the heliostat. The method describes the flux density distribution with an empirical function of the mentioned parameter, then takes integration to obtain the total energy. Two integration methods—direct and convolution integral—are commonly used. The former calculates the flux density distribution on the receiver plane directly. The convolution integral method first calculates the solar flux at the image plane and then projects it to the receiver plane [7]. Typically, the analytical approach approximates these effects through a convolution-based integration method, due to its lower computational resource requirement. For the flat heliostats, Walzel et al. employed the 2D Hermite function to statistically simulate the flux density distribution on the receiver, which is reflected by a flat heliostat [8]. Lipps and Walzel proposed a numerical technique for computing the flux density distribution of a heliostat with arbitrary shapes, considering shading and blocking effects [9]. Although the calculation result is of high precision, the calculation speed is slower than that of the Hermite function. For a focusing heliostat, Collado et al. (1986) proposed the UNIZAR model in the integral form through image plane transition for a focusing heliostat, which is the convolution of several Gaussian error functions [10]. The HFCAL model [11], an analytical flux density function, developed by Michael Kiera in the early 1980s, has the ability to compute efficiently solar flux density, which is much simpler and more accurate than the UNIZAR model [12]. He et al. proposed the iHFLCAL model as an improvement of the HFLCAL model, which considers shadowing and blocking effects [13].

Ray-tracing is a common approach for studying heliostats [14] and concentrated solar collectors [15]. The ray-tracing approach uses the principle of tracing a large number of rays incident on a reflector and reflected onto the receiving panel. The calculation of solar intensity can be executed with a remarkable level of adaptability to cater for diverse circumstances, and the process of programming is uncomplicated, leading to the acquisition of dependable outcomes [16]. The utilization of the Monte Carlo ray-trace (MCRT) method, while potentially reducing calculation complexity, does come with a drawback in the form of increased computational resource and time consumption requirements for achieving greater result accuracy compared to the convolution-based method [17]; therefore, it is not suitable for system optimization [18]. According to the states of the ray-tracing, three MCRT methods are available: forward ray-tracing, backward ray-tracing, and bidirectional ray-tracing. The forward ray-tracing approach involves the generation of rays originating from the Sun, subsequently reflected by the heliostat and ultimately received by the designated receiver. Several software applications have been created through the implementation of this approach, such as SolTrace [19], Tonatiuh [20], and Tracer [21], among others. In the backward ray-tracing method (BRT), the rays are generated from the receiver, traced in reverse to the heliostats and then to the Sun. Several studies have applied this method to estimate flux density distribution [22–24]. However, in this method, numerous rays from the receiver do not hit the heliostat arising from the fact that the size of the receiver surface is much larger than that of the heliostat, resulting in computations that are inefficient and unproductive. In the method of bidirectional ray-tracing, the rays emanate from the heliostats, resulting in improved efficiency of the MCRT technique due to the intersections between the rays and the determined heliostats. STRAL is a commercial bidirectional ray-tracing simulation tool with multithreading techniques [25].

Analytical methods offer computational expediency and simplicity through their application of concise mathematical expressions, providing foundational insights into system behavior. However, their reliance on simplifying assumptions introduces limitations in capturing the intricacies of real-world complexities, particularly in scenarios involving complex geometries. On the other hand, the ray-tracing method, while computationally

intensive, excels in accuracy and flexibility, accommodating intricate systems and diverse scenarios. Its realistic representation of light ray behavior enhances its applicability. This increased complexity and precision come at the cost of longer computation times, making ray-tracing a more intensive computation resource. The choice between these methods hinges on system complexity, speed requirements, and accuracy priorities. A judicious blend of both approaches may be deployed to strike a balance between computational efficiency and precision in CSP simulations.

The aim of this study was to simplify the calculations while simultaneously reducing the computation time, all without compromising the accuracy of the results. The stated objective can be achieved by integrating the advantages and disadvantages of each method. Instead of using the ray-tracing method, this study employs the forward curve tracing technique to track the position of sunlight as it strikes various components of the CSP system. The intensity and energy of the incident radiation are calculated using the convolution-based integration method, leveraging the principles of parametric design for model development.

Parametric design utilizing Rhinoceros® and Grasshopper® constitutes a potent methodology that endows the designer with the capacity to generate intricate and dynamic 3-D models by establishing interdependencies between diverse design parameters. Rhino 7 is a software application designed for three-dimensional modeling, whereas Grasshopper functions as a visual programming plug-in that facilitates algorithmic modeling within Rhino. Using Rhinoceros and Grasshopper for design has become increasingly popular in building design [26–30], landscape/urban design [31–34], and other creative fields [35–38].

Rhinoceros® and Grasshopper's parametric design can offer a sophisticated approach to CSP flux-distribution evaluation, emphasizing the need for validation and resource considerations in solar energy system simulations. With dynamic modeling and adaptability, Grasshopper enables real-time exploration of design parameter effects on flux distribution, especially in handling complex CSP geometries. The integrated simulation tools provide insights into spatial aspects, aiding designers in optimizing sunlight concentration. Parametric sensitivity analyses within Grasshopper facilitate the identification of influential parameters for iterative refinement. Despite its potential, accuracy hinges on model precision, necessitating validation against real-world data. Efficient use of computational resources is critical, particularly for complex simulations.

To the best of our understanding, there has been no previous reporting on the employment of parametric design methodology to simulate and visualize radiative flux density distributions. The objective of this study was to generate new methodology, curve tracing (instead of ray-tracing), using the heliostat curve tracing parametric model (HCTPM). This model, in conjunction with both analytical and ray-tracing advantages, elucidates the radiative flux density distributions on receiver planes generated by flat heliostats, and can be applied to various shapes of mirrors. This study will initiate a flexible and visualized alternative method to further analyze and evaluate the performance of other aspects of the CSP system. The following are the contributions of this research as a summary:

- Integration of sustainable design practices: The approach can be applied to optimize heliostat configurations, enabling better use of solar resources and aligning with sustainable design principles in renewable energy infrastructure.
- Energy efficiency optimization: This model enhances the accuracy of solar energy distribution on heliostats and receivers, contributing to more efficient energy capture in concentrated solar power (CSP) systems, thus promoting sustainable energy solutions.
- Flexibility in adapting to varying solar conditions: The model's adaptability to different Sun angles and heliostat positions ensures that the CSP systems can be optimized for maximum sustainability across various environmental conditions.
- Support for long-term sustainability goals: By improving energy balance and reducing losses, this model contributes to the broader objective of achieving net zero emissions and reducing dependence on fossil fuels.

2. Model Conceptual Design

The Sun is not a point source but appears as a "disk" when viewed from the earth. Solar intensity across the Sun disk is non-uniform, and the flux density varies along the radial direction. Points closer to the center will have a higher flux density (W/m^2) compared to those farther away. As illustrated, it appears as circular curves around the center point, as shown in Figure 1. Each circle at the same radius is formed by the continuous arrangement of numerous points of ray sources with the same flux density.

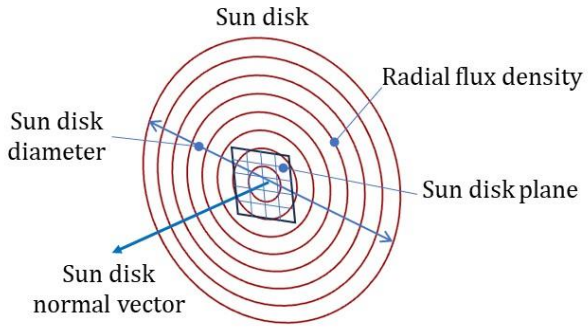


Figure 1. Sun disk.

When these curves or segments of the curves are transferred and projected onto the mirrors, their shapes and lengths change according to the angles at which they strike the mirror. Except in cases where both the Sun disk plane and the mirror plane are flat, and the normal vector of the radiation source is perpendicular to the receiver plane, the size, shape, and distribution of the radial flux density will remain unchanged, as shown in Figure 2. However, the energy of these curves remains constant (assuming there is no loss during transmission through the atmosphere or absorption by the surface of the equipment), resulting in changes in their flux density.

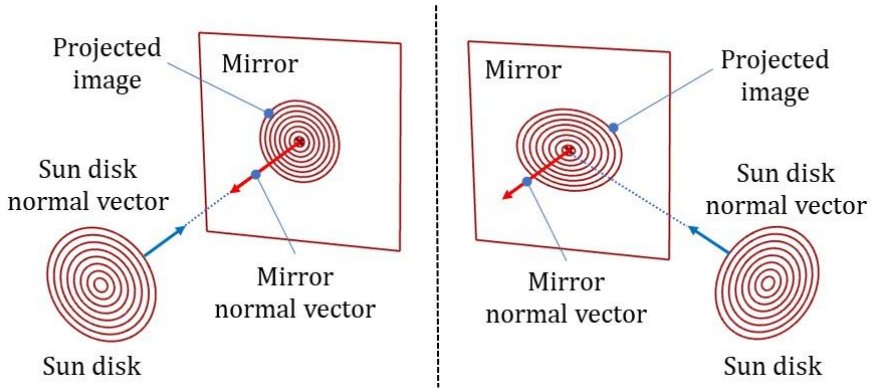


Figure 2. Projected image on mirror with scenario of Sun disk normal vector being perpendicular to the mirror plane (**left**) and non-perpendicular to mirror plane (**right**).

When radiation is reflected from the mirror to the receiver, the changes in the size and shape of the reflected image, which is projected onto the receiver, depend on both the reflection angle from the mirror and the incidence angle at the receiver. When the reflection angle from the mirror equals the incidence angle at the receiver, the size and shape of the image on the receiver will remain unchanged (Figure 3a). However, when the reflection angle from the mirror is greater or less than the incidence angle at the receiver, the size and shape of the image on the receiver will tend to decrease or increase, respectively (Figure 3a,c).

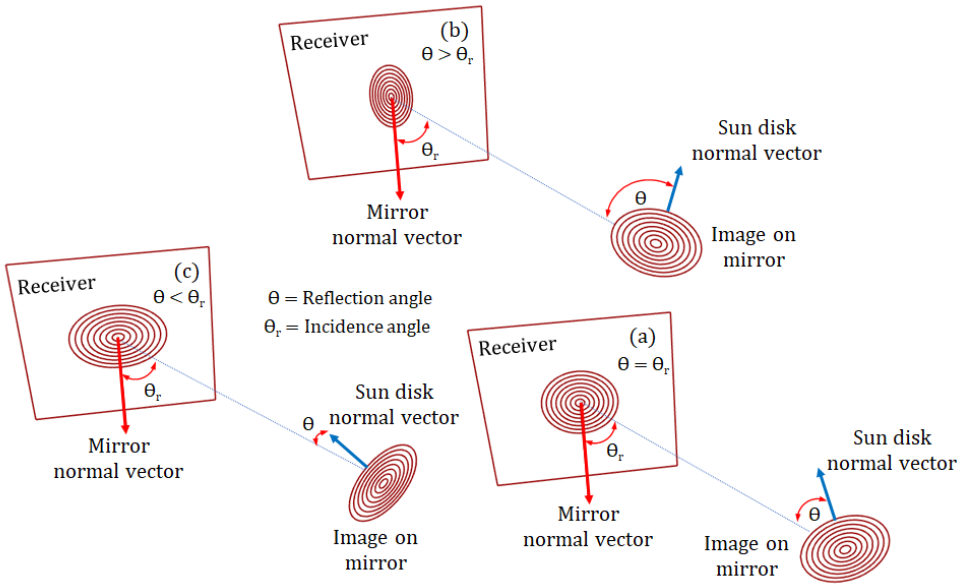


Figure 3. Projected images on the receiver and their deformation in different scenarios. (**a**) $\theta = \theta_r$ (**b**) $\theta > \theta_r$ (**c**) $\theta < \theta_r$.

If a curve or a segment of a curve does not strike the mirror or receiver, it will be excluded from the energy calculation and counted as spill loss, as shown in Figure 4.

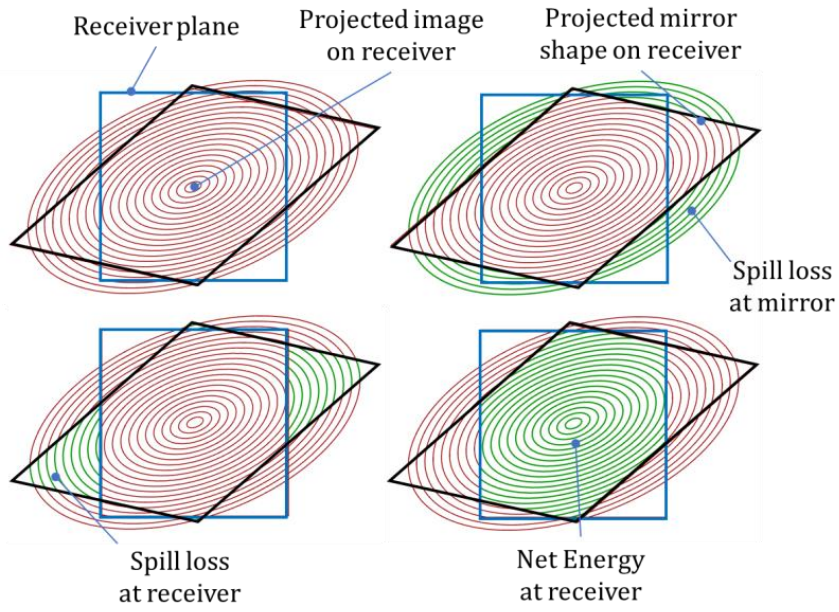


Figure 4. Spill loss at mirror, at receiver and received net energy.

Only the portion of the energy that strikes the receiver is considered in the net energy calculation. The energy of each curve is evaluated based on the initial energy from the Sun disk and adjusted according to the flux density coefficient, depending on how it impacts the various components, as described above. Then, the volume under the flux distribution surface is determined to obtain the net energy, as shown in Figure 5. This process separates the tracking of flux density and the position transfer of the curves in the initial step, reducing the number of rays that need to be tracked. Once the positions of the curves on the receiver are determined, both aspects are considered together. This approach results in accurate outcomes and provides flexibility in adjusting various parameters, while also conserving computational resources.

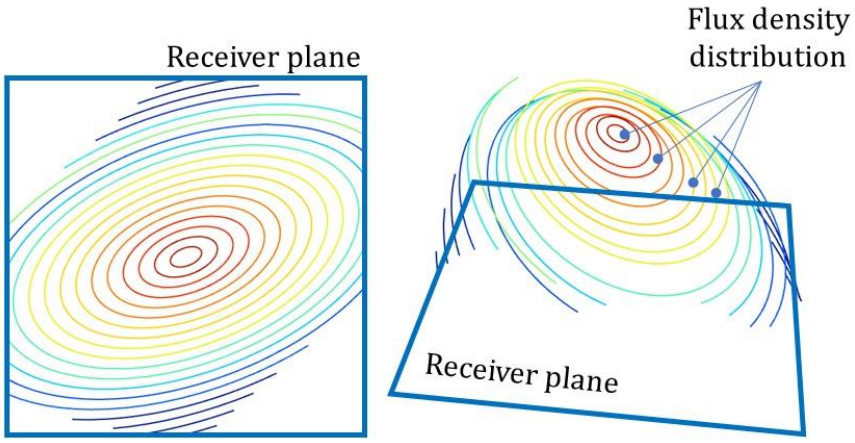


Figure 5. Flux distribution and net energy on receiver plane; top-view (**left**), perspective (**right**).

3. Methodology

3.1. Model Structure

The HCTPM model in this study represents a CSP system with flat mirrors and a solar-tracking mechanism. Adjustable parameters such as project coordinates, date and time, and the size and shape of the mirrors and receivers are used as input data for the model (a). The day of year (DOY) and hour of year (HOY) are calculated from the input date and time to determine the solar insolation (b) and Sun position (c). The Sun's flux density (d) along the radial direction, which depends on the selected equations and variables, is combined with the solar insolation and Sun position to create the Sun disk (e) and its plane.

The field layout determines the positions of the mirrors and the receiver. The shape and size of the mirrors (f) can be specified by adjusting variables such as the number of sides of the polygon and the area of the mirror. By considering the above information together, the mirror plane (g) is obtained. The receiver plane can be created based on data from the receiver design (i), which includes adjustable parameters such as the size, orientation, and tilt angle of the receiver.

The total energy of the Sun disk (o) can be calculated by integrating the flux density to obtain the total energy volume. When the Sun disk is projected onto the mirror plane (k) and the changes in flux density due to the cosine loss at the mirror are considered, the resulting flux density on the mirror (m) is obtained. By integrating this flux density, the total energy incident on the mirror (p) is determined. The difference between the energy from the Sun disk and the energy incident on the mirror represents the spill loss at the mirror (r).

When the projected image on the mirror is projected onto the receiver plane, the resulting projected image on the receiver (l) is obtained. The flux density on the receiver (n) is determined by considering the cosine loss at the mirror, attenuation loss, and cosine loss at the receiver. Similar to the total energy from the Sun disk and the energy on the mirror, the net energy on the receiver (q) can be calculated by integrating the flux density over the entire area of the receiver. Subsequently, this information can be used to calculate the spill loss at the receiver (s). The structure of model is explained as Figure 6.

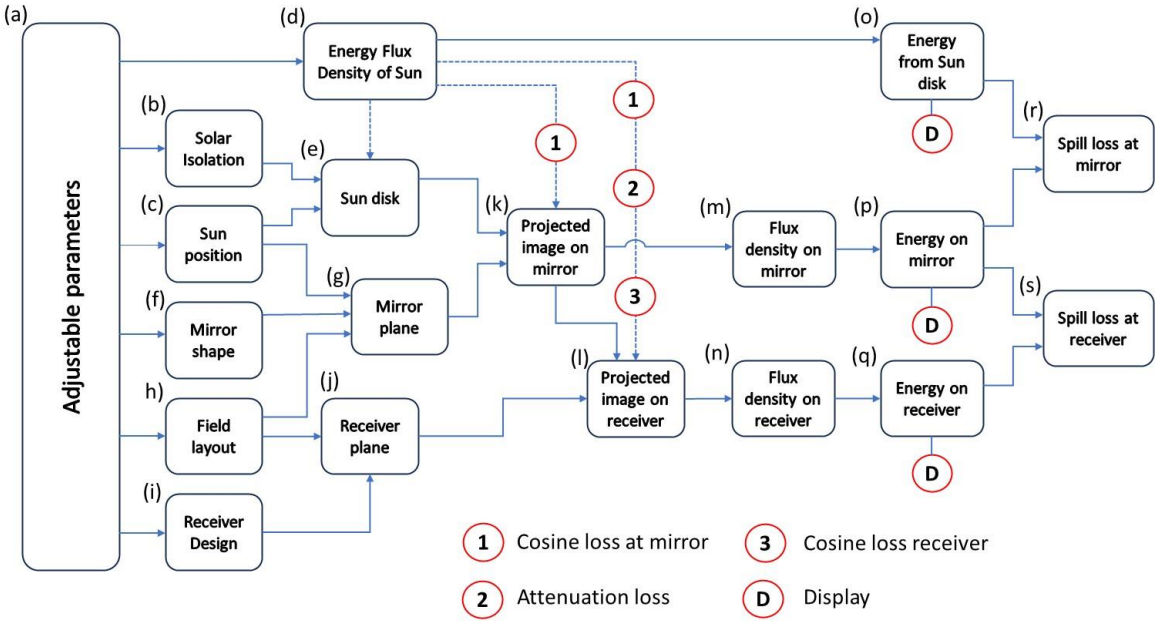


Figure 6. Parametric model structure.

3.2. Location

In the model used in this study, the location is a variable that can be specified and adjusted only through the latitude coordinates, as the position of the Sun at different times of the day does not depend on the longitude coordinates. However, if there is a need to import specific local climate data from a database for evaluation, both latitude and longitude coordinates must be specified. This study does not consider local climatic variables such as temperature, humidity, cloud cover, and the amount of particulate matter in the atmosphere, all of which affect the intensity of solar radiation.

3.3. Field Layout

There are several common heliostat field layout types used in concentrated solar power (CSP) plants: rectangular/cartesian, radial, spiral, etc. In the present study, the reflector was arranged in a radial manner. This specific arrangement proves to be highly suitable for CSP plants of smaller scale and topographies that are not uniform. The radial configuration provides a degree of flexibility in conforming to atypical land shapes and may also confer an aesthetic allure [39]. The polar angle, measured from the angle made with the north direction, and the radial distance from the tower, range up to 100 m, are the two adjustable parameters. The positioning of reflector/mirror on the field can be determined using the aforementioned parameters, as exemplified in Figure 7. For instance, position 1 is designated as [NE 40°, D 100], and position 2 is [NW 60°, D 80], and so forth.

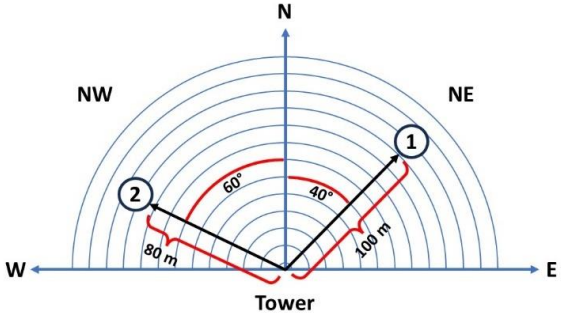


Figure 7. Heliostat positioning in the field.

3.4. Receiver Tower

The receiver tower is where the concentrated sunlight from the heliostats is focused and converted into thermal energy. The height of the tower used in this study is fixed at 25 m (however, this parameter is adjustable). At the top of the tower is the receiver, which contains a heat-absorbing material or working fluid. The receiver of the present model is 8 m × 8 m square flat plate, oriented towards the north and capable of modifying its tilt angle within the range of 0–90 degrees.

3.5. Reflector/Mirror

The reflector is the most crucial component of a heliostat, as it reflects and concentrates sunlight onto a specific target. There are two main types of reflectors based on their shape: flat and curved (or canting). The curvature of the reflector allows for improved focusing and concentration of sunlight, resulting in higher energy densities at the target. However, it is more complex and expensive to manufacture and requires precise shaping and alignment [40,41]. Despite the potential drawbacks of the flat mirror configuration, such as limitations in achieving high concentration ratios and precise sunlight focusing onto a specific target, the current research model employs this design due to its inherent simplicity and the potential for future development into a curved reflector model. The reflector for the present model can be chosen from among geometric shapes such as a rectangle, circle, or polygon, with the area of the selected shape up to a maximum of 128 m^2. The center of the geometric figure is located at the reflector's corresponding point in the field. In this model, the reflector is assumed to have no slope error, resulting in the reflected rays always being parallel.

3.6. Sun Position

The system used in this study is a Sun-tracking reflector. The configuration of the heliostat tracking system relies entirely on the position of the Sun and the position of the reflector. In order to comprehend comprehensively the position of the Sun in relation to a flat surface on the Earth at any given point in time, it is imperative to possess an understanding of additional angles grounded on the Earth's coordinates, including the following: decline angle (δ), hour angles (ω), north celestial pole (or NCP) latitude (ϕ), solar altitude (α_s), zenith angle (θ_z), and solar azimuth (Y_s), as shown in Figure 8.

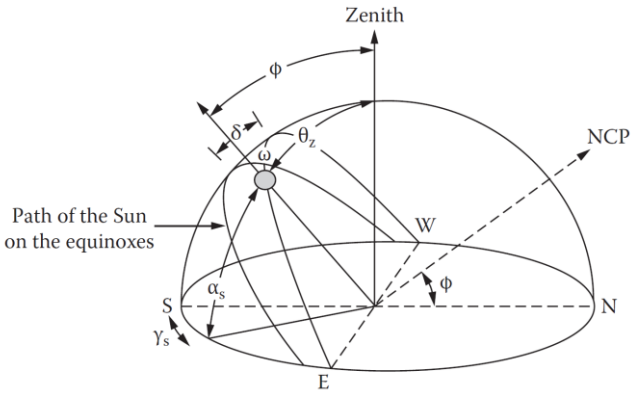


Figure 8. Position of the Sun in relation to the Earth's surface.

The decline angle equals the following [40]:

$$\delta = 23.45\, sin(360(284 + N)/365) \quad (1)$$

where N is the day of the year with 1 Jan as N = 1.

The hour angle (ω) is the angular distance between the Sun's position at a particular time and its highest position for that day when crossing the local meridian at the solar

noon. The hour angle changes by 15° per hour and moves through 360° over the course of the day. The hour angle is defined to be zero at solar noon, a negative value before crossing the meridian, and a positive after crossing. Therefore,

$$\omega = 15(TSV - 12) \tag{2}$$

where TSV is the solar time in 24 h.

The α_s, changing hourly and daily, can be calculated in terms of δ, ϕ, and ω by using the next set equation [41]:

$$\alpha_s = \sin^{-1}(\sin\phi\sin\delta + \cos\phi\cos\delta\cos\omega) \tag{3}$$

Therefore, the zenith angle can be defined as below:

$$\theta_z = \cos^{-1}(\sin\phi\sin\delta + \cos\phi\cos\delta\cos\omega) \tag{4}$$

The solar azimuth angle, Y_s, can be calculated in terms of δ, ϕ, and ω following Braun and Mitchell's (1983) [42] formulation:

$$Y_s = C_1C_2Y_s' + C_3((1 - C_1C_2)/2)180 \tag{5}$$

where Y_s' is a pseudo solar azimuth angle, Y_s', for the first or fourth quadrant. The calculation of C_1 determines whether or not the Sun is within the first or fourth quadrants and above the horizon:

$$C_1 = 1\begin{cases} if|\omega| < \omega_{WE} \\ or \\ if|\tan\delta/\tan\phi| > 1 \end{cases}, -1 \text{ otherwise} \tag{6}$$

where ω_{WE} is the hour angle when the Sun is due east or west and can be obtained as

$$\cos\omega_{WE} = \tan\delta/\tan\phi \tag{7}$$

Constant C_2 and C_3 can be evaluated by the following:

$$C_2 = 1\ if\ \phi(\phi - \delta) \geq 0, -1 \text{ otherwise} \tag{8}$$

$$C_3 = 1\ if\ \omega \geq 0, -1 \text{ otherwise} \tag{9}$$

3.7. Sun-Shape

The distribution of solar intensity across the Sun disk is non-uniform, exhibiting a decrease in magnitude towards its periphery. A statistical comparison can be drawn to a normal distribution with different standard deviations, given that both distributions exhibit the same root mean square deviation from the central ray [11]. The flux density distribution of the Sun disk can be modeled as a circular Gaussian pattern. Since the flux spot center is the origin of the Sun disk system and distributed along the radial direction, the radial power distribution density function is given as follows [43]:

$$F(r) = 2\pi r \times I \times e^{-\frac{r^2}{2\sigma^2}} \tag{10}$$

where σ is the Sun shape error

Therefore, the radial power per length or flux density on radial r is

$$f(r) = I \times e^{-\frac{r^2}{2\sigma^2}} \tag{11}$$

Solar insolation (I) is the quantity of solar radiation received at a certain point on the surface of the earth. Solar insolation can be calculated using the following formula:

$$I = I_0(\cos\theta_z) \tag{12}$$

where I_0 is the solar constant, assumed to be 1000 watt/m^2 for this study. However, this model can integrate real climate data, specifically using measured solar insolation values, which can be imported into the model as an ewp file.

The total power of circular Gaussian flux (P_{tot}) over the whole Sun disk is as follows:

$$\int_0^\infty F(r)dr = 2\pi I\sigma^2 = P_{tot} \tag{13}$$

and $F(r)$ reaches to its maximum value at $r = \sigma$.

The disparity between the Sun-shape employed in the present model and previous literature studies is that the later employed the "elliptical" Gaussian distribution to depict the reflected image on, whereas in this study, "circular" Gaussian distribution was applied to generate the Sun disk as the source of solar rays, then projected onto the mirror and receiver.

3.8. Tracking and Mirror Plane

Vector techniques can be utilized to obtain the tracking angles for each reflector, in conjunction with their corresponding incidence angles, as shown in Figure 9. The zenith, east, and north $(z,\ e,\ n)$ directions serve as the appropriate coordinates, with an origin of O located at the base of the receiving tower. Figure 9 shows the proposed Cartesian coordinate system; point A $(z_0,\ 0,\ 0)$ corresponds to the location in space where the receiver is placed and point B $(z_1,\ e_1,\ n_1)$ is the location of a mirror close to the ground.

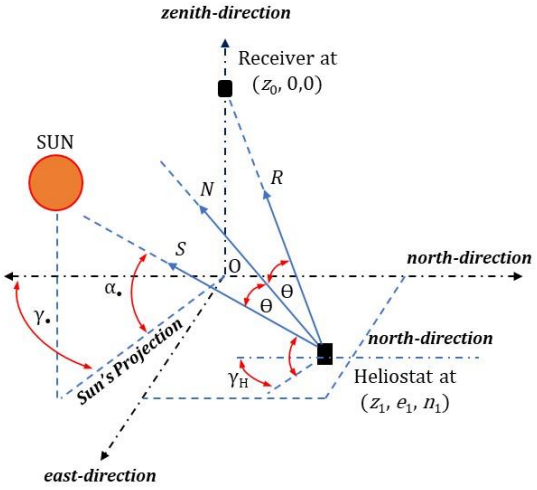


Figure 9. Reflector tracking vector.

To determine the mirror normal ($\vec{N}$), two vectors must be defined: a vector representing the direction of the Sun's ray hitting the mirror ($\vec{S}$) and redirection of the Sun's ray toward the point A, receiver ($\vec{R}$). These three vectors can be represented by the following equations [44]:

$$\vec{S} = S_z\hat{i} + S_e\hat{j} + S_n\hat{k} \tag{14}$$

$$\vec{N} = N_z\hat{i} + N_e\hat{j} + N_n\hat{k} \tag{15}$$

$$\vec{R} = R_z\hat{i} + R_e\hat{j} + R_n\hat{k} \tag{16}$$

The $\vec{S}$—components can be written in terms of solar altitude (α_s) and azimuth (Y_s) as

$$S_z = \sin \alpha_s \tag{17}$$

$$S_e = \cos \alpha_s \sin Y_s \tag{18}$$

$$S_n = \cos \alpha_s \cos Y_s \tag{19}$$

and the $\vec{R}$ vector is defined as

$$\vec{R} = \left((z_0 - z_1)\hat{i} - e_1\hat{j} - n_1\hat{k}\right) / \left(\sqrt{(z_0 - z_1)^2 + e_1^2 + n_1^2}\right) \tag{20}$$

By the law of specular reflection, which must be applied, the angle of incidence is equal to the angle of reflection. The scalar point between the vectors of $\vec{S}$ and $\vec{R}$ results in a practical expression that involves the incidence angle as follows:

$$\cos 2\theta = \vec{S} \cdot \vec{R} \tag{21}$$

The mirror normal can be found by adding the incidence and reflection vectors and dividing by the appropriate scalar quantity. This gives

$$\vec{N} = \left((R_z + S_z)\hat{i} + (R_e + S_e)\hat{j} + (R_n + S_n)\hat{k}\right) / 2\cos\theta \tag{22}$$

3.9. Cosine Loss

An essential factor contributing to the reduction of solar concentrator efficiency stems from the inability of mirror to consistently align perpendicular to the incoming solar rays. In instances where mirrors reflect off-axis, the visible surface area of the mirror from the perspective of the Sun is diminished in accordance with the cosine of the angle of incidence [45–47]. The cosine efficiency (η_{cos}) can be evaluated as the following [48]:

$$\eta_{cos-H} = \cos\theta = \text{area of Sun disk plane} / \text{area of image on mirror} \tag{23}$$

The aforementioned principle is similarly implemented in instances wherein the reflected ray deviates from perpendicularity with respect to the receiver plan relation with the cosine efficiency of the mirror:

$$\eta_{cos-R} = \cos\theta_r \text{ area of image on mirror} / \text{area of image on receiver} \tag{24}$$

where θ_r is the incidence angle of the reflected rays on the receiver.

3.10. Atmospheric Attenuation

During the trajectory from the mirror to the receiver, the reflected rays undergo the influence of atmospheric attenuation. The attenuation losses are contingent on the separation between the heliostat and the receiver. Moreover, these losses are subject to certain meteorological conditions, such as visibility. The atmospheric attenuation efficiency (η_{atm}) can be ascertained via the following expression [49]:

$$\eta_{atm} = \begin{cases} 0.99321 - 0.0001176\, D + 1.97 \times 10^{-8}\, D^2\,, & D \leq 1000 \\ exp(-0.0001106D)\,, & D > 1000 \end{cases} \tag{25}$$

where D is the distance from reflector to receiver. However, if other parameters related to visibility assessment, like cloud cover, dust, and humidity, are available, they can be directly used to evaluate attenuation loss.

3.11. Flux Density Distributions and Energy Calculation on Receiver

In order to display the flux distribution and calculate the energy incident on the receiver using the HCTPM model, the Sun disk and the mirror shape are projected onto the receiver system, as shown in Figure 10a.The flux density of a curve incident on different planes can be evaluated under the assumption that the flux density changes by cosine loss, and the losses due to atmospheric attenuation between the heliostat and the receiver. Thus, the flux density of any radial curve on the heliostat ($f(r)_H$) and receiver ($f(r)_R$) plane can be calculated using the following equations:

$$f(r)_H = \eta_{cos-H} \times f(r) \tag{26}$$

$$f(r)_R = \eta_{atm} \times \eta_{cos-R} \times \eta_{cos-H} \times f(r) \tag{27}$$

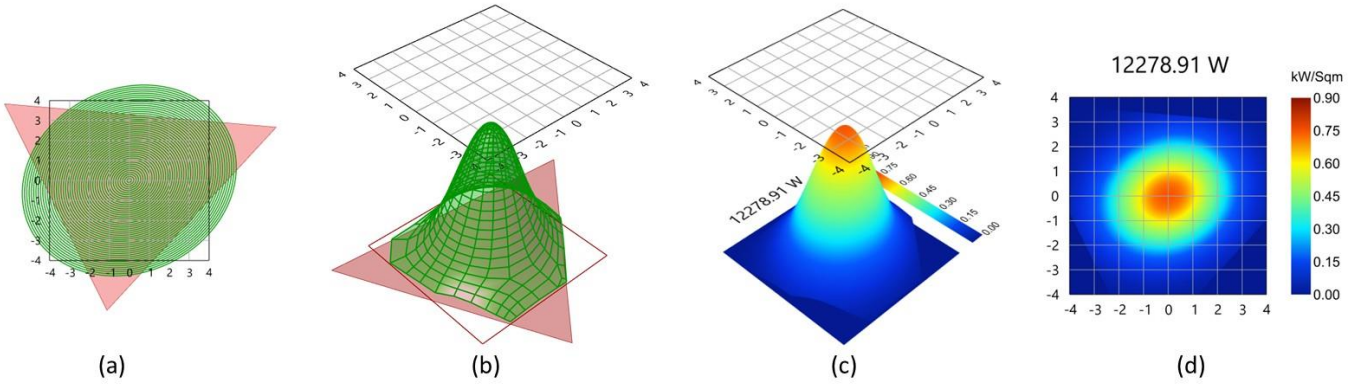


Figure 10. Flux density distributions and energy calculation on receiver. (**a**) projected curve on receiver plan (**b**) mesh surface of flux density (**c**) flux density color gradient (**d**) top view.

Subsequently, the level of each curve is adjusted according to its flux density and from the mesh surface. The parts of the mesh that lie outside the boundaries of the projected mirror shape and the receiver plane are trimmed away before calculating the volume under the surface of the mesh to obtain the energy incident on the receiver (Figure 10b). Different flux densities are represented by a color gradient, with areas of the receiver surface that do not receive any energy indicated by the lowest color level (Figure 10c). A top view of the results is illustrated in Figure 10d.

In cases where the results on the mirror are considered, the process can be applied similarly. The difference lies in the fact that the mesh surface of the energy on the mirror is generated from the flux distribution that only considers the cosine loss on the mirror, then this mesh surface is trimmed according solely to the boundaries of the mirror plane.

The HCTPM were constructed in the Grasshopper® canvas (Figure 11) and visualized in the Rhinoceros® (Rhino 7) screen (Figure 12). The Grasshopper canvas serves as the main workspace where users develop parametric designs through visual programming. It allows components to be dragged and connected, forming algorithms that define complex geometries. These components, each representing operations like geometry creation, data processing, or mathematical functions, are connected by wires that pass data between them. Each component has inputs and outputs, facilitating the flow of information within the design. Several types of components are used, ranging from primitive components that create basic shapes (points, lines, surfaces) to complex data manipulation tools that handle lists and trees. For added flexibility, Grasshopper allows custom scripting with Python or C#, enabling more advanced functionality beyond the default components. Grasshopper employs a sophisticated data tree system to manage complex parametric data, enabling simultaneous processing of multiple datasets. Once the design is complete, it can be "baked" into Rhino 7, turning the parametric geometry into a static model for further manipulation.

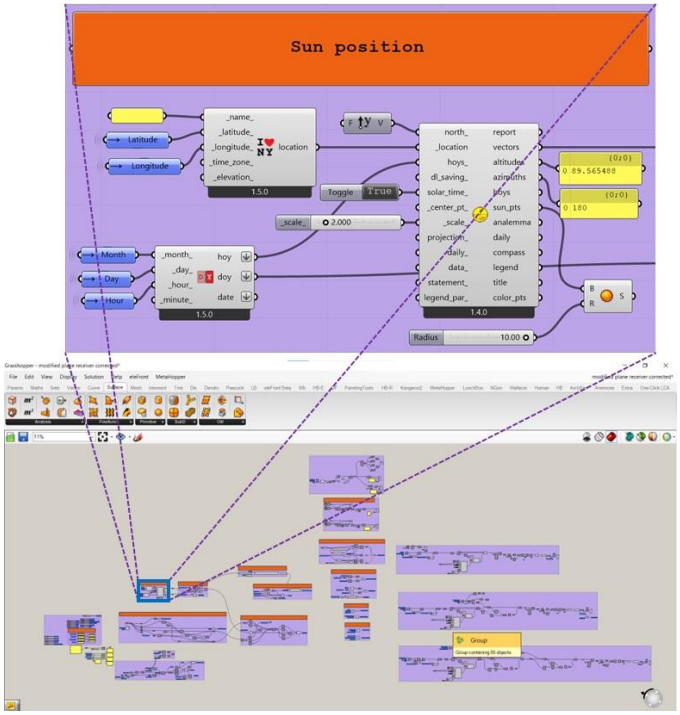


Figure 11. Grasshopper canvas.

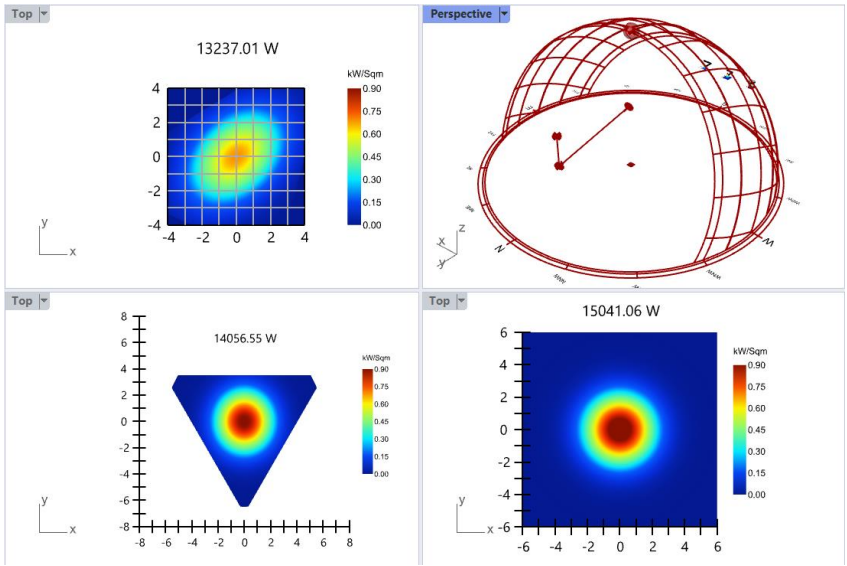


Figure 12. Rhinoceros screen.

4. HCTPM Model Validation

The model validation in this study was conducted by comparing the simulation results with previous literature, examining the energy balance, and assessing the trends, feasibility, and outcomes in response to changing parameters.

4.1. Radius of Sun Disk and Standard Deviation Employed in the Gaussian Distribution

In the HCTPM model, the size of the Sun disk and the Sun-shape error (standard deviation) significantly influence the solar energy received, which serves as a fundamental factor in the energy analysis. Accurate determination of these parameters is crucial, as they directly affect the simulation outcomes and the overall energy yield calculations. The radius of the Sun disk and the standard deviation employed are interrelated parameters

within the context of circular Gaussian distribution. The radius of the Sun disk refers to the radius of the circular projection of the Sun on a plane perpendicular to the vector representing the Sun's position. Essentially, it establishes the boundary where the solar power per unit area becomes zero at any given point and time. This boundary, however, is contingent on the value of the standard deviation employed in the Gaussian equation. When the Sun shape error is small, it indicates a narrower power distribution along the radial axis, resulting in a reduced boundary area and low total power. Conversely, a larger Sun-shape error value corresponds to a broader power distribution along the radial axis, leading to an expanded boundary area and higher total power. Notably, determination of Sun shape error requires empirical measurements in specific environmental contexts, including, time of day, geographical location, and prevailing weather conditions. In this study, we explored the sensitivity arising from variations in the radius of the Sun disk and Sun shape error variables, specifically by varying the Sun shape error value within the range of 1 to 2. This range is commonly employed in the literature as an initial parameter range for general initial design considerations.

Figure 13 illustrates the relationship between the percentage of energy obtained from the Sun disk at various radii (ranging from 50% to 100% of total power) and the Sun shape error. This analysis was conducted under a solar insolation value of approximately 1000 W/m^2. It is evident that the percentage of power increases linearly as the radius expands within the power percentage range of 50% to 75%. However, beyond the 75% power range, this relationship deviates from linearity, a deviation that becomes particularly pronounced as the power approaches 100%.

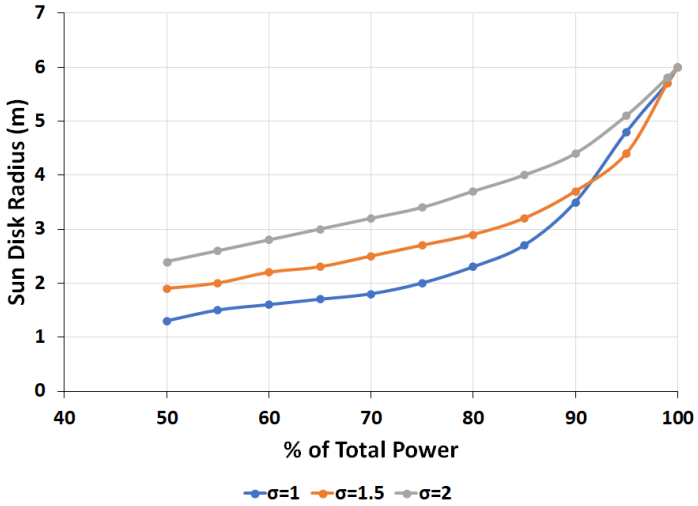


Figure 13. The proportion of energy from the Sun disk for varying Sun shape errors: Latitude = 23°, Date = 21 June, Time = 12.00, Position = [N 0°, D 30].

The energy of the Sun disk with a Sun shape error in the range of 1–2 converges to 100% when the radius of the Sun disk is approximately 6 m. This observation indicates that the optimal size of the Sun disk for a Sun shape error within this range can be set to a maximum value not exceeding 6 m. However, selecting a value smaller than 6 m will result in a reduced energy value for the Sun disk. Notably, Sun disks with higher Sun shape errors exhibit greater sensitivity to changes in size compared to those with lower Sun shape errors.

The Sun disk image from this study was compared with the results of Guo and Wang [43], which used the same values for "Solar isolation" and "Sun shape error," as shown in Figure 14. It was found that the Sun disk with a radius of 4.4 m in this study (Figure 14c) exhibits similar characteristics and energy levels to the Sun disk from the mentioned literature, even though the radius used in this study captures 95% of the total energy. Using a radius that is too small for this Sun shape error (Figure 14a) shows

that the outer boundary of the Sun disk is clearly defined from the background due to significant trimming of the outer part, resulting in a noticeable reduction in energy. However, increasing the radius to capture nearly 100% of the energy does not significantly alter the appearance of the Sun disk compared to the literature, and the energy levels remain similar.

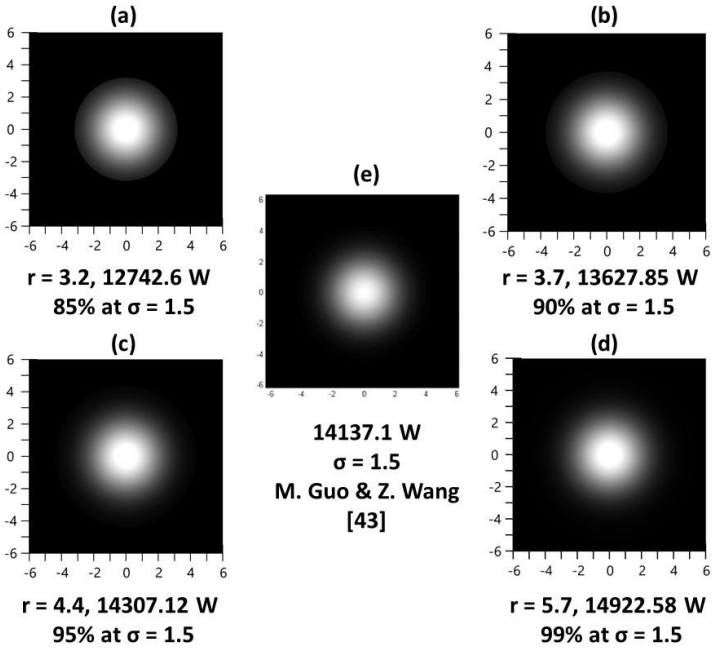


Figure 14. Compare the image of the Sun disk from this study with previous research [43].

This study also compares the receiver image resulting from Sun disks of various sizes and energy levels from other models in previous research [50]. As shown in Figure 15, the projected image on the receiver in this study has characteristics and size similar to the results of the HFLCAL model, which is based on the Gaussian and Tonatiuh models that employ the ray-tracing method. The findings suggest that the model developed in this study demonstrates a comparable level of accuracy to existing models, showcasing its reliability. Additionally, the model's flexibility is highlighted by its ability to adapt to a range of scenarios. This adaptability is influenced by the specific attributes of the Sun disk and the configuration of mirrors and the receiver, allowing for versatile application across various conditions.

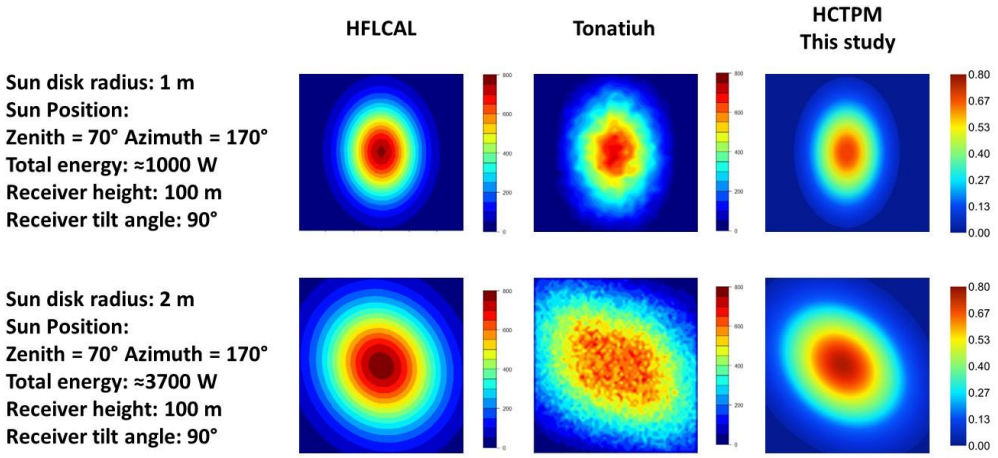


Figure 15. Comparing the result image on receiver with existing models.

4.2. Examining the Accuracy of HCTPM Model via Energy Balancing

The energy from the Sun disk that strikes the mirrors and the receiver, assuming no spill losses and no energy losses during transmission or absorption by various surfaces, should remain constant, equating to the initial energy from the Sun disk. In this study, we analyzed the deviations from energy balancing when the energy received by the mirrors and receiver diverges from the expected values.

For this analysis, the Sun disk at solar noon on the summer solstice is simulated to impact mirror positions at [N 0°, D30] and [NE 45°, D 30], with reflections directed towards a receiver situated at a height of 25 m and a tilt angle of 60°. Both the mirrors and the receiver have an area of 64 square meters each. Subsequently, the Sun shape error is adjusted within the range of 1–2, and the Sun radius is varied within the range of 1–3 m. This ensures the complete projection of the Sun disk's image on both the mirrors and the receiver, with shape alterations but no spill losses. Furthermore, attenuation loss is excluded from consideration in this study. The resulting deviations can be elucidated by referring to Figure 16 as described below.

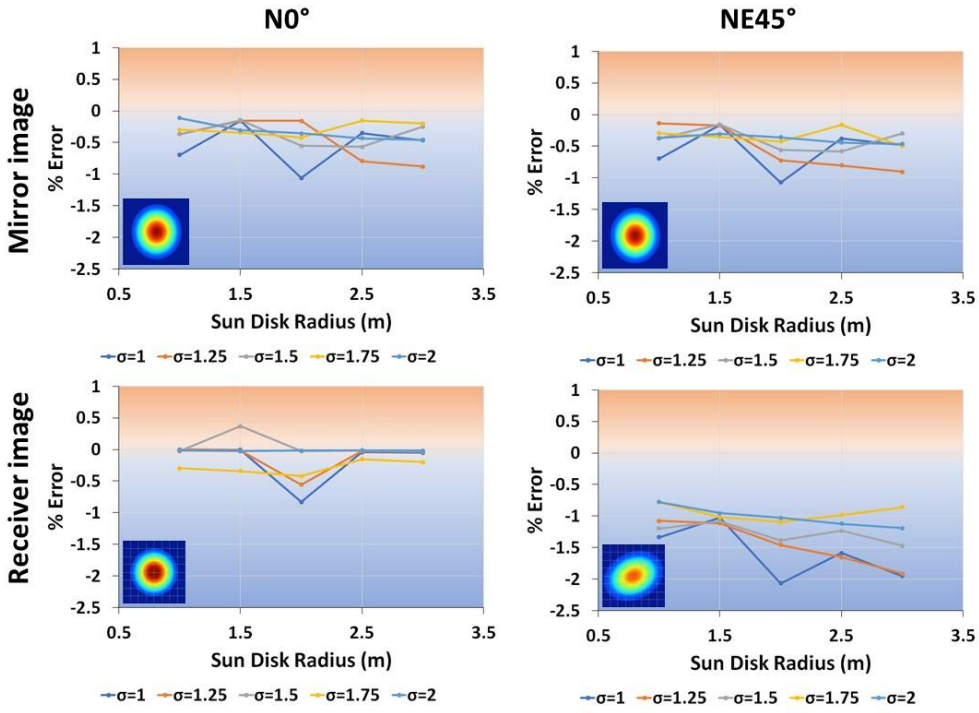


Figure 16. Analysis of energy balancing deviation on mirror and receiver.

It was found that the deviation values in all cases, whether at the mirrors or the receiver, ranged from −2.5% to 1%. The smallest average deviation occurred on the receiver reflecting from the mirror positioned at [N0°, D30], while the largest deviation was observed on the receiver reflecting from the mirror positioned at [NE 45°, D 30]. The larger deviations may result from the elliptical shape of the image, which differs from the circular shape of the Sun disk, potentially causing inaccuracies in the volume calculations for energy determination. Additional evidence supporting the relationship between the deviations and the shape of the image is that the projected images of the Sun disk on the mirrors in both cases were also elliptical but more circular in appearance. Therefore, the deviations were moderate and quite similar.

The deviation from energy balancing tends to increase as the Sun shape error decreases. This phenomenon may be due to the lower Sun shape error leading to a higher flux density, concentrated at the center of the image, thus increasing sensitivity to deviations. However, for more circular projections, this effect is less pronounced compared to elliptical projections.

Additionally, an increase in the radius of the Sun disk tends to result in greater deviations, which are particularly noticeable when the projection has an elliptical shape.

4.3. Examining the Trends, Feasibilities, and Outcomes in Response to Changing Parameters

This section analyzes whether the trends in the model's outcomes align with reality. The shape and size of the Sun disk of the summer solstice at latitude 23° N are set to constant values, with a Sun shape error of 1.5 and a radius of 5.7 m (consistent with the results analyzed in the Sun disk analysis section). These are projected onto a rectangular mirror with an area of 64 square meters, placed at a fixed distance of 30 m from the receiver. The rectangular shape of the mirror facilitates the observation of the impact angles at various positions. The image on the mirror is then reflected onto a square receiver with an area of 64 square meters, positioned at a height of 25 m and with a tilt angle of 60°. Subsequently, the mirror's position and the time of light exposure are varied, and the resulting images on the receiver are recorded from different scenarios, as shown in Figure 17.

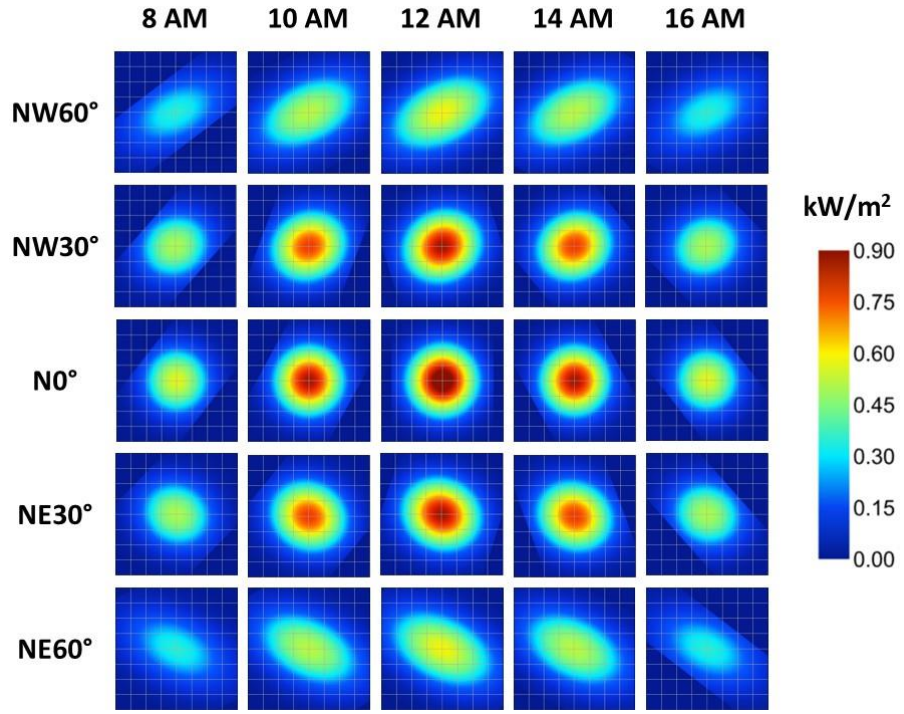


Figure 17. Responses of model parameter varying.

From the results, the alignment with reality can be explained as follows: When the mirror is positioned directly north of the receiver, the shape of the Sun disk appearing on the receiver remains a fairly complete circle, due to the narrow reflection angle from the mirror to the receiver. As the mirror's position deviates further from the north (both westward and eastward), the shape of the projection on the receiver gradually transforms into a more elliptical shape, with the orientation of the elliptical axis depending on the mirror's direction. This transformation from a circular to an elliptical shape as the mirror's position changes does not alter the amount of received energy (assuming no spill occurs), but it reduces the flux density. Changing the time of exposure does not affect the shape of the Sun disk projection, but it does influence the edges of the projection as seen on the receiver, which is a reflection of the mirror's image. Additionally, the received energy and flux density on the receiver vary with time.

4.4. Examining Effect of Mirror Shape and Spill Loss

One of the significant advantages of the HCTPM model is its flexibility to adjust the size and shape of the mirror, which allows for a variety of projections on the receiver beyond just circular or elliptical forms. This adaptability is demonstrated in Figure 18. The simulation parameters, including the date, time, and receiver characteristics, remain consistent with the previous sections, with the Sun shape error and radius set to 1.5 and 5.7 m, respectively, to highlight the influence of the mirror shape more clearly.

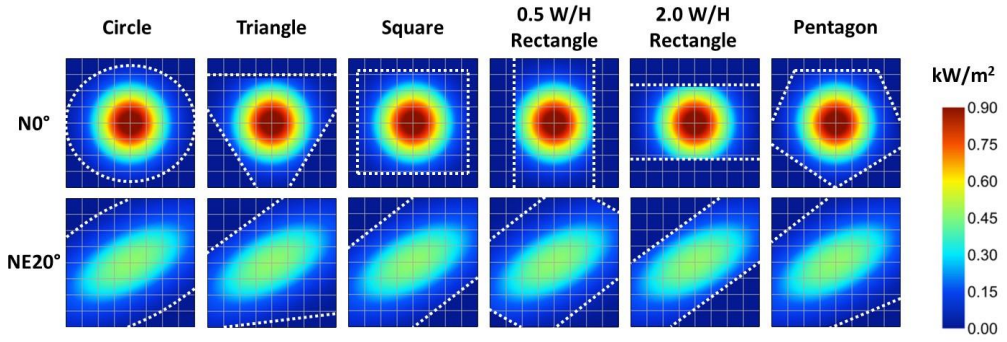


Figure 18. Projected images on receiver with different mirror shapes.

By maintaining a constant mirror area of 48 square meters and altering the mirror shape, the mirror was positioned to yield circular and elliptical projections on the receiver at positions [N 0°] and [NE 20]. It was observed that the Sun disk's shape projected onto the receiver remained consistent irrespective of the mirror shape. However, the edges of the projection, defined by the mirror's shape, varied accordingly (as indicated by the white dashed lines).

This characteristic is particularly advantageous as it enables the assessment of spill losses on both the mirror and the receiver when the size and shape of the mirror are modified. Such evaluations are instrumental in optimizing the design of mirrors, ensuring appropriate shapes and sizes for different mirror positions.

The analysis of spill loss on both the mirror and the receiver was conducted by configuring the Sun disk to have a larger size and broader energy distribution (Sun shape error = 2 and radius = 6). The mirrors were then positioned at [N 0°] and [NE 30°], and the resulting spill loss was systematically recorded as the mirror size varied between 10 to 90 square meters and the mirror shape was altered between a 0.7 W/H ratio rectangle and a circle.

The results indicate that increasing the size of the mirror significantly reduces the spill loss on the mirror itself, with this trend being consistent regardless of the mirror's shape or position. However, increasing the mirror size leads to a higher spill loss on the receiver, particularly when the mirror's position deviates significantly from the north. Analyzing the total spill loss reveals that it tends to decrease as the mirror size increases (with the receiver size remaining constant). Nevertheless, this decreasing trend becomes less pronounced as the spill loss on the receiver increases, which is notably evident when the mirror's position deviates further from the north (Figure 19a,b). When the mirror is positioned directly north, the majority of the total spill loss is attributable to the spill loss on the mirror. These findings can benefit the determination of the optimal mirror and receiver sizes in other scenarios.

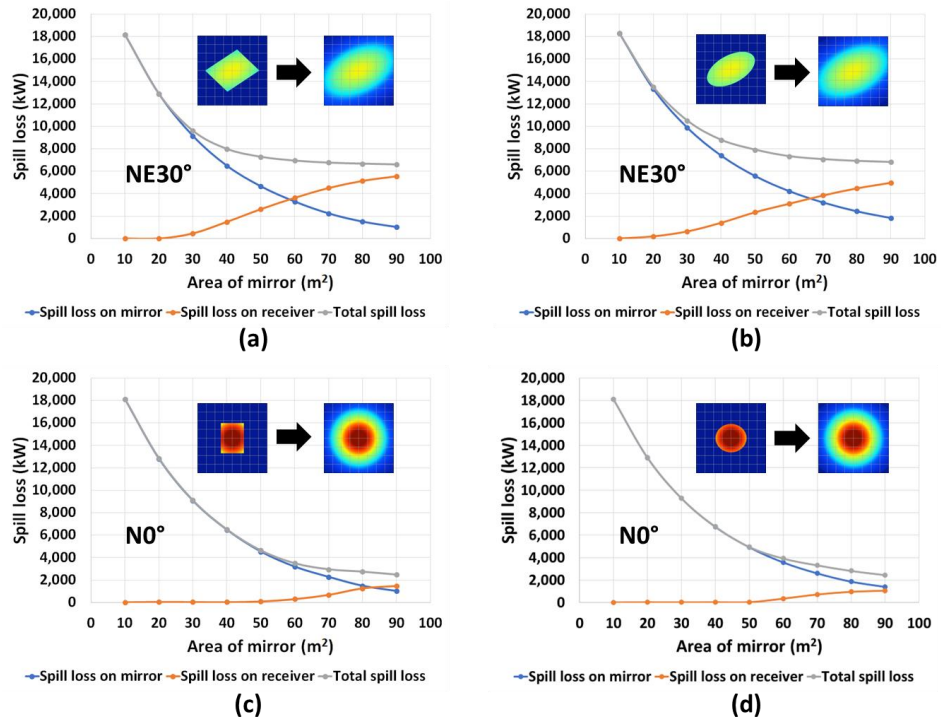


Figure 19. Spill loss analysis. (**a**) NE30° with rectangular mirror (**b**) NE30° with circular mirror (**c**) N0° with rectangular mirror (**d**) N0° with circular mirror.

The above analysis demonstrates one advantage of the HTPCM model, which is its ability to analyze the shape of the mirrors as well as the suitability of the mirror size in relation to the receiver size. The appropriate sizing of both the mirrors and the receiver increases the energy efficiency in the design while also reducing the investment costs.

5. Conclusions

This study demonstrates the advantages of the HCTPM model in simulating solar energy distribution for concentrated solar power (CSP) systems. The HCTPM model leverages the strengths of previous models, allowing users to observe the flux distribution of projected images on both the Sun disk on mirrors and receivers. By tracking the changes in curves on various components, the model reduces the amount of data required for analysis, thereby saving computing resources while maintaining calculation accuracy.

The HCTPM model is highly flexible, accommodating various parameters such as date, time, and project location. It can incorporate real climatic data if available. Parameters related to the Sun disk, mirrors, and receivers can be easily adjusted, enhancing the model's applicability to different scenarios. When compared with other models, HCTPM shows consistency in both energy quantification and the characteristics of the Sun disk. This includes models based on ray-tracing and Gaussian principles. The accuracy of the HCTPM model, verified through energy balancing tests, shows deviations within 2.5%. This minor deviation may result from the assumption that the energy level remains constant across all points on the curve, even if the curve shape deviates from a circle. However, this deviation is negligible compared to spill losses.

Unlike other models, HCTPM can analyze spill losses on both mirrors and receivers. It can also adjust the shape of mirrors, which aids in further analysis of blocking or shadowing effects due to different mirror arrangements in the field. Although initially designed for heliostat systems with flat mirrors and planar receivers, the parametric design of HCTPM allows for potential future development. It can be adapted to evaluate flux distribution from other concentrating devices such as parabolic dishes or troughs and curved receivers capable of omnidirectional light reception. These results pave the way for further research

and development, potentially expanding the application of the HCTPM model to a broader range of solar energy collection devices and configurations. The ability to simulate and optimize complex solar energy systems accurately will play a crucial role in the ongoing efforts to make solar energy a more viable and efficient renewable energy source.

Author Contributions: Conceptualization, P.U.; Methodology, P.U.; Validation, H.P. Writing—original draft preparation, P.U.; Review and Editing, H.P. All authors have read and agreed to the published version of the manuscript.

Funding: This research received no external funding.

Institutional Review Board Statement: Not applicable.

Informed Consent Statement: Not applicable.

Data Availability Statement: Data are contained within the article.

Conflicts of Interest: The authors declare no conflicts of interest.

References

1. Lilliestam, J.; Labordena, M.; Patt, A.; Pfenninger, S. Empirically observed learning rates for concentrating solar power and their responses to regime change. *Nat. Energy* **2017**, *2*, 17094. [CrossRef]
2. Kangogo, T.; Kabini, K. A Review of Heliostat Technologies used in Concentrated Solar Power Plants. In Proceedings of the Sustainable Research and Innovation Conference, Pretoria, South Africa, 20–24 June 2022.
3. Lin, X.; He, C.; Huang, W.; Zhao, Y.; Feng, J. GPU-based Monte Carlo ray tracing simulation considering refraction for central receiver system. *Renew. Energy* **2022**, *193*, 367–382. [CrossRef]
4. Cruz, N.; Salhi, S.; Redondo, J.; Álvarez, J.; Berenguel, M.; Ortigosa, P. Hector, a new methodology for continuous and pattern-free heliostat field optimization. *Appl. Energy* **2018**, *225*, 1123–1131. [CrossRef]
5. Elsayed, M.; Fathalah, K. Solar flux density distribution using a separation of variables/superposition technique. *Renew. Energy* **1994**, *4*, 77–87. [CrossRef]
6. He, C.; Duan, X.; Zhao, Y.; Feng, J. An analytical flux density distribution model with a closed-form expression for a flat heliostat. *Appl. Energy* **2019**, *251*, 113310. [CrossRef]
7. Sánchez-González, A.; Santana, D. Solar flux distribution on central receivers: A projection method from analytic function. *Renew. Energy* **2015**, *74*, 576–587. [CrossRef]
8. Walzel, M.; Lipps, F.; Vant-Hull, L. A solar flux density calculation for a solar tower concentrator using a two-dimensional hermite function expansion. *Sol. Energy* **1977**, *19*, 239–253. [CrossRef]
9. Lipps, F.; Walzel, M. An analytic evaluation of the flux density due to sunlight reflected from a flat mirror having a polygonal boundary. *Sol. Energy* **1978**, *21*, 113–121. [CrossRef]
10. Collado, F.; Gómez, A.; Turégano, J. An analytic function for the flux density due to sunlight reflected from a heliostat. *Sol. Energy* **1986**, *37*, 215–234. [CrossRef]
11. Schwarzbözl, P.; Pitz-Paal, R.; Schmitz, M. Visual HFLCAL—A Software Tool for Layout and Optimisation of Heliostat Fields. In Proceedings of the SolarPACES 2009, Berlin, Germany, 15–18 September 2009.
12. Collado, F. One-point fitting of the flux density produced by a heliostat. *Sol. Energy* **2010**, *84*, 673–684. [CrossRef]
13. He, C.; Zhao, Y.; Feng, J. An improved flux density distribution model for a flat heliostat (iHFLCAL) compared with HFLCAL. *Energy* **2019**, *189*, 116239. [CrossRef]
14. Wei, X.; Lu, Z.; Yu, W.; Wang, Z. A new code for the design and analysis of the heliostat field layout for power tower system. *Sol. Energy* **2010**, *84*, 685–690. [CrossRef]
15. Cheng, Z.; He, Y.; Cui, F.; Du, B.; Zheng, Z.; Xu, Y. Comparative and sensitive analysis for parabolic trough solar collectors with a detailed Monte Carlo ray-tracing optical model. *Appl. Energy* **2014**, *115*, 559–572. [CrossRef]
16. Huang, W.; Yu, L.; Hu, P. An analytical solution for the solar flux density produced by a round focusing heliostat. *Renew. Energy* **2019**, *134*, 306–320. [CrossRef]
17. Cheng, Z.; He, Y.; Cui, F. A new modelling method and unified code with MCRT for concentrating solar collectors and its applications. *Appl. Energy* **2013**, *101*, 686–698. [CrossRef]
18. Lipps, F. A numerical approach to the flux density integral for reflected sunlight. *Sol. Energy* **1980**, *24*, 461–469. [CrossRef]
19. Wendelin, T. SolTRACE: A new optical modeling tool for concentrating solar optics. In Proceedings of the International Solar Energy Conference, Kohala Coast, HI, USA, 15–18 March 2003.
20. Blanco, M.; Amieva, J.; Mancillas, A. The Tonatiuh Software Development Project: An open source approach to the simulation of solar concentrating systems. In Proceedings of the ASME International Mechanical Engineering Congress and Exposition, Orlando, FL, USA, 5–11 November 2005.
21. Wang, Y.; Asselineau, C.; Coventry, J.; Pye, J. Optical performance of bladed receivers for CSP systems. In Proceedings of the Energy Sustainability, ASME 2016 Power and Energy Conference, Charlotte, NC, USA, 26–30 June 2016.

22. Daly, J. Solar concentrator flux distributions using backward ray tracing. *Appl. Opt.* **1979**, *18*, 2696–2699. [CrossRef]
23. Pancotti, L. Optical simulation model for flat mirror concentrators. *Sol. Energy Mater. Sol. Cells* **2007**, *91*, 551–559. [CrossRef]
24. Chiesi, M.; Vanzolini, L.; Scarselli, E.; Guerrieri, R. Accurate optical model for design and analysis of solar fields based on heterogeneous multicore systems. *Renew. Energy* **2013**, *55*, 241–251. [CrossRef]
25. Belhomme, B.; Pitz-Paal, R.; Schwarzbözl, P.; Ulmer, S. A new fast ray tracing tool for high-precision simulation of heliostat fields. *J. Sol. Energy Eng.* **2009**, *131*, 031002. [CrossRef]
26. de Sousa Freitas, J.; Cronemberger, J.; Soares, R.; Amorim, C. Modeling and assessing BIPV envelopes using parametric Rhinoceros plugins Grasshopper and Ladybug. *Renew. Energy* **2020**, *160*, 1468–1479. [CrossRef]
27. Eltaweel, A.; Su, Y. Controlling venetian blinds based on parametric design; via implementing Grasshopper's plugins: A case study of an office building in Cairo. *Energy Build.* **2017**, *139*, 31–43. [CrossRef]
28. Aliakbari, K.; Ebrahimi-Moghadam, A.; Ildarabadi, P. Investigating the impact of a novel transparent nano-insulation in building windows on thermal comfort conditions and energy consumptions in different climates of Iran. *Therm. Sci. Eng. Prog.* **2021**, *25*, 101009. [CrossRef]
29. Mahroo, H.; Vafamehr, M. Structural optimization of four designed roof modules: Inspired by Voronax grid shell structures. *Front. Archit. Res.* **2023**, *12*, 129–147. [CrossRef]
30. Hussain, M.; Zheng, B.; Chi, H.; Hsu, S.; Chen, J. Automated and continuous BIM-based life cycle carbon assessment for infrastructure design projects. *Resour. Conserv. Recycl.* **2023**, *190*, 106848. [CrossRef]
31. Taleb, H.; Musleh, M. Applying urban parametric design optimisation processes to a hot climate: Case study of the UAE. *Sustain. Cities Soc.* **2015**, *14*, 236–253. [CrossRef]
32. Amado, M.; Poggi, F. Solar urban planning: A parametric approach. *Energy Procedia* **2014**, *48*, 1539–1548. [CrossRef]
33. van Ameijde, J.; Ma, C.; Goepel, G.; Kirsten, C.; Wong, J. Data-driven placemaking: Public space canopy design through multi-objective optimisation considering shading, structural and social performance. *Front. Archit. Res.* **2022**, *11*, 308–323. [CrossRef]
34. Abdollahzadeh, N.; Biloria, N. Urban microclimate and energy consumption: A multi-objective parametric urban design approach for dense subtropical cities. *Front. Archit. Res.* **2022**, *11*, 453–465. [CrossRef]
35. Li, S.; Nguyen-Xuan, H.; Tran, P. Digital design and parametric study of 3D concrete printing on non-planar surfaces. *Autom. Constr.* **2023**, *145*, 104624. [CrossRef]
36. Aramburu, A.; Calderon-Uriszar-Aldaca, I.; Puente, I. Parametric modelling of 3D printed concrete segmented beams with rebars under bending moments. *Case Stud. Constr. Mater.* **2023**, *18*, e01910. [CrossRef]
37. Girardet, A.; Boton, C. A parametric BIM approach to foster bridge project design and analysis. *Autom. Constr.* **2021**, *126*, 103679. [CrossRef]
38. Sulpizio, C.; Fiore, A.; Demartino, C.; Vanzi, I.; Briseghella, B. Optimal design criteria for form-finding of double-curved surfaces. *Procedia Manuf.* **2020**, *44*, 28–35. [CrossRef]
39. Hinkley, J.; Hayward, J.; Curtin, B.; Wonhas, A.; Boyd, R.; Grima, C.; Tadros, A.; Hall, R.; Naicker, K. An analysis of the costs and opportunities for concentrating solar power in Australia. *Renew. Energy* **2013**, *57*, 653–661. [CrossRef]
40. Blanco-Muriel, M.; Alarcón-Padilla, D.; López-Moratalla, T.; Lara-Coira, M. Computing the solar vector. *Sol. Energy* **2001**, *70*, 431–441. [CrossRef]
41. Qiu, Z.; Li, P. Solar Energy Resource and Its Global Distribution. In *Solar Photovoltaic Power Optimization*; Springer: Singapore, 2021; pp. 15–35.
42. Braun, J.; Mitchell, J. Solar geometry for fixed and tracking surfaces. *Sol. Energy* **1983**, *31*, 439–444. [CrossRef]
43. Guo, M.; Wang, Z. On the analysis of an elliptical Gaussian flux image and its equivalent circular Gaussian flux images. *Sol. Energy* **2011**, *85*, 1144–1163. [CrossRef]
44. Foster, R.; Ghassemi, M.; Cota, A. *Solar Energy: Renewable Energy and the Environment*; CRC Press: Boca Raton, FL, USA, 2009.
45. Ho, C.; Brian, D. Review of high-temperature central receiver designs for concentrating solar power. *Sustain. Energy Rev.* **2014**, *29*, 835–846. [CrossRef]
46. Zeghoudi, A.; Debbache, M.; Hamidat, A. Contribution to minimizing the cosine loss in a thermodynamic solar tower power plant by a change in the target position. *Eur. J. Electr. Eng.* **2017**, *6*, 367–374. [CrossRef]
47. Mahmoud, M.; Khudheyer, A.; Abdul-Ghafoor, Q. Minimizing the Cosine Loss in a Solar Tower Power Plant by a Change in the Heliostat Position and Number. *Int. J. Eng. Adv. Technol. (IJEAT)* **2020**, *9*, 2302–2304. [CrossRef]
48. Wei, X.; Lu, Z.; Yu, W.; Zhang, H.; Wang, Z. Tracking and ray tracing equations for the target-aligned heliostat for solar tower power plant. *Renew. Energy* **2011**, *36*, 2687–2693. [CrossRef]
49. Eddhibi, F.; Amara, M.; Balghouthi, M.; Guizani, A. Optical study of solar tower power plants. *J. Phys. Conf. Ser.* **2015**, *596*, 012018. [CrossRef]
50. García, L.; Burisch, M.; Sanchez, M. Spillage estimation in a heliostats field for solar field optimization. *Energy Procedia* **2015**, *69*, 1269–1276. [CrossRef]

Disclaimer/Publisher's Note: The statements, opinions and data contained in all publications are solely those of the individual author(s) and contributor(s) and not of MDPI and/or the editor(s). MDPI and/or the editor(s) disclaim responsibility for any injury to people or property resulting from any ideas, methods, instructions or products referred to in the content.